How vinculin regulates force transmission

David W. Dumbauld[a,b], Ted T. Lee[a,b], Ankur Singh[a,b], Jan Scrimgeour[b,c], Charles A. Gersbach[a,b], Evan A. Zamir[a,b], Jianping Fu[d], Christopher S. Chen[e], Jennifer E. Curtis[b,c], Susan W. Craig[f], and Andrés J. García[a,b,1]

[a]Woodruff School of Mechanical Engineering, [b]Petit Institute for Bioengineering and Bioscience, and [c]School of Physics, Georgia Institute of Technology, Atlanta, GA 30332; [d]Department of Mechanical Engineering, University of Michigan, Ann Arbor, MI 48109; [e]Department of Bioengineering, University of Pennsylvania, Philadelphia, PA 19104; and [f]Department of Biological Chemistry, Johns Hopkins Medical School, Baltimore, MD 21205

Edited by James A. Spudich, Stanford University School of Medicine, Stanford, CA, and approved May 1, 2013 (received for review September 18, 2012)

Focal adhesions mediate force transfer between ECM-integrin complexes and the cytoskeleton. Although vinculin has been implicated in force transmission, few direct measurements have been made, and there is little mechanistic insight. Using vinculin-null cells expressing vinculin mutants, we demonstrate that vinculin is not required for transmission of adhesive and traction forces but is necessary for myosin contractility-dependent adhesion strength and traction force and for the coupling of cell area and traction force. Adhesion strength and traction forces depend differentially on vinculin head (V_H) and tail domains. V_H enhances adhesion strength by increasing ECM-bound integrin–talin complexes, independently from interactions with vinculin tail ligands and contractility. A full-length, autoinhibition-deficient mutant (T12) increases adhesion strength compared with V_H, implying roles for both vinculin activation and the actin-binding tail. In contrast to adhesion strength, vinculin-dependent traction forces absolutely require a full-length and activated molecule; V_H has no effect. Physical linkage of the head and tail domains is required for maximal force responses. Residence times of vinculin in focal adhesions, but not T12 or V_H, correlate with applied force, supporting a mechanosensitive model for vinculin activation in which forces stabilize vinculin's active conformation to promote force transfer.

cell adhesion | fibronectin

Integrin-mediated adhesion to ECM provides mechanical anchorage and signals that direct cell migration, proliferation, and differentiation (1, 2), processes central to tissue organization, maintenance, and repair. After ligand binding, integrins cluster into focal adhesion (FA) complexes that transmit adhesive and traction forces (3–6). FAs consist of integrins and actins separated by a ∼40 nm core that includes cytoskeleton (CSK) elements, such as vinculin and talin, and signaling molecules, including focal adhesion kinase and paxillin (7). FAs mediate responses to internal and external stresses by modulating force transfer between integrins and the CSK (8–10). This function has been likened to a "mechanical clutch" between an engine and transmission (11).

On the basis of its structure and binding partners, vinculin represents an attractive candidate for orchestrator of clutch function. Vinculin consists of a globular head (V_H) linked to a tail domain (V_T) by a proline-rich strap (12). V_H contains talin, α-actinin, and α- and β-catenin binding sites; actin, paxillin, and phosphatidylinositol 4,5-bisphosphate (PIP2) binding sites are in V_T; and vasodilator-stimulated phosphoprotein (VASP), actin-related protein 2/3 (Arp2/3), and vinexin binding sites reside in the proline-rich region. Interactions with these partners are regulated by an autoinhibited conformation arising from high-affinity intramolecular head–tail binding (13, 14). Activation of vinculin can occur by simultaneous binding to talin and actin or α-catenin and actin (15, 16). Vinculin is activated when localized to FAs (17). Vinculin forms a complex with β_1 integrin and talin (18) and interacts with talin to enhance integrin activation (19). Therefore, vinculin has the required molecular properties to mechanically link integrin–ECM complexes to the actomyosin CSK in a regulated manner.

In addition to studies on vinculin's effects on muscle function (20–22), which may or may not be related to its mechanical functions, vinculin's role in force transmission has largely been inferred from studies with vinculin-deficient cells showing altered FA assembly and aberrant migration (23, 24). For instance, V_H drives FA growth via interactions with talin, whereas V_T colocalizes to actin filaments (25), but whether these interactions mediate force transfer is unknown. Vinculin-deficient cells do exhibit reduced cortical CSK stiffness and adhesive force (26, 27), and vinculin is a force-carrying component between FAs and the CSK (28). Although these studies implicate vinculin in force transmission, few such measurements have been made, and some have provided evidence against a role of vinculin in force coupling (29). Moreover, possible roles played by vinculin domains and autoinhibition in mechanotransduction are largely unexplored.

In this study we used stable lines of vinculin-null cells expressing vinculin mutants and two force-measuring platforms to directly analyze whether and how vinculin transmits force. We found that although vinculin is not essential for transmission of traction and adhesive forces, it regulates the coupling of cell area and traction force and is required for myosin contractility-dependent traction forces and adhesion strength. In addition, we found that adhesion strength and traction forces depend to different extents on V_H and V_T, but maximal force transmission requires the talin/α-actinin–binding site on V_H, physical connection of V_H and V_T, and release of the autoinhibitory head–tail interaction. Finally, we discovered a linear relationship between the traction force at an FA and the residence time for vinculin at that FA, providing evidence for a mechanosensitive model for vinculin activation in which forces applied across vinculin maintain the molecule in its active conformation to increase residence times at FAs to promote force transfer.

Results

Stable Expression of Vinculins in Vinculin-Null Cells. We expressed WT and mutant vinculins fused to enhanced green fluorescent protein (eGFP) in vinculin-null cells using a tetracycline-regulated retroviral system (Fig. 1*A* and Fig. S1*A*). This strategy has major advantages over routine approaches using transient expression in vinculin-expressing cells: (*i*) experiments are based on the same cell population, eliminating batch-to-batch variability in expression levels; (*ii*) reexpression of target vinculins in cells lacking endogenous expression avoids confounding effects of endogenous vinculin; and (*iii*) the retroviral system has high transduction efficiencies, resulting in a polyclonal population of engineered cells and avoiding issues associated with clonal lines. We applied this system to two vinculin-null mouse embryonic fibroblast lines [MEF1 (15, 30) and MEF2 (13, 23, 31)] to rule out artifacts of a particular line. After transduction, WT vinculin-eGFP positive cell populations were enriched by FACS. Western blotting confirmed expression of vinculin constructs in both lines of

---

Author contributions: D.W.D., S.W.C., and A.J.G. designed research; D.W.D., T.T.L., A.S., and J.S. performed research; C.A.G., E.A.Z., J.F., C.S.C., J.E.C., and S.W.C. contributed new reagents/analytic tools; D.W.D., T.T.L., A.S., J.S., and A.J.G. analyzed data; and D.W.D., A.S., J.E.C., S.W.C., and A.J.G. wrote the paper.

The authors declare no conflict of interest.

This article is a PNAS Direct Submission.

[1]To whom correspondence should be addressed. E-mail: andres.garcia@me.gatech.edu.

This article contains supporting information online at www.pnas.org/lookup/suppl/doi:10.1073/pnas.1216209110/-/DCSupplemental.

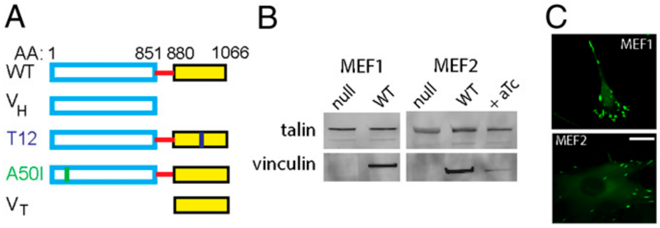

Fig. 1. Vinculin-null cells engineered to express vinculin variants. (*A*) Vinculin variants fused to eGFP: WT, head domain (V_H), auto-inhibition mutant (T12), talin-binding mutant (A50I), and tail domain (V_T). (*B*) Western blot analysis of engineered cell lines confirmed expression of vinculin constructs. Vinculin expression was repressed in presence of anhydrotetracycline (aTc, 100 ng/mL). (*C*) eGFP-vinculin localized to FAs for both MEF1- and MEF2-derived lines. (Scale bar, 10 μm.)

transduced vinculin-null MEFs (Fig. 1*B*). Expression levels for WT were comparable to levels in vinculin$^{+/+}$ cells derived from littermate controls. Culturing MEF2 cells in the presence of anhydrotetracycline significantly repressed levels of vinculin-eGFP expression. eGFP-vinculin localized to FAs, demonstrating proper function for the expressed proteins (Fig. 1*C*).

To investigate the contributions of vinculin domains to force transmission, cell lines expressing eGFP-vinculin mutants were derived from MEF1 vinculin-null cells. We first examined two mutants: (*i*) a molecule comprising only V_H (1–851) and lacking most of the proline-rich strap and actin-binding tail, and (*ii*) a full-length variant (T12) with mutations along the head–tail interface that reduce head–tail binding affinity 100-fold and render the molecule in an active conformation that can readily bind talin and actin (Fig. 1*A*). These mutants have been characterized for their binding to talin and actin and recruitment to FAs (13, 25, 31). Equivalent expression levels were observed among cell lines (Fig. S1*B*). V_H-expressing cells were more round than WT-expressing cells, and the V_H construct localized to large radial FAs (Fig. S1*C*). T12-expressing cells displayed more and larger FAs than WT-expressing cells (Fig. S1*C*). These phenotypes are consistent with observations for transiently transfected cells (13, 25).

Vinculin Activation Increases Traction Forces and Regulates Coupling Between Cell Area and Total Traction Force. We used microfabricated postarray deflection devices (mPADs) to measure traction forces. When seeded overnight onto fibronectin (FN)-coated mPADs, cells spread and developed FAs (Fig. 2*A* and Fig. S2*A*). T12-expressing cells exhibited higher spread areas compared with other lines, and V_H-expressing cells spread more than null but not WT-expressing cells (Fig. 2*B*). Treatment with blebbistatin (20 μM, 30 min), an inhibitor of myosin contractility, reduced cell area for null, WT-, and T12-expressing cells but not V_H-expressing cells. We measured post deflections for null and vinculin-expressing lines. Fig. 2*A* and Fig. S2*A* present images (*Upper*) for FN-coated posts (red) and eGFP-vinculin (green) recruited to FAs, with the cell outlined in yellow and force vectors (cyan, *Lower*) calculated from post deflections. The magnitude of traction forces varied significantly across a single cell, with the highest forces at the cell periphery (Fig. 2*A* and Fig. S2*A*). Fig. 2*C* presents box-whisker plots for the total traction force per cell, which represents the sum of the magnitudes of the force vectors for each cell and is commonly used for reporting traction forces (32). Traction forces are dynamic, and the data in Fig. 2*C* represent a "snapshot" of the traction forces in a cell population at equilibrium (overnight culture). Vinculin-null cells generate considerable traction forces (~100 nN), indicating that vinculin is not required for force transmission at FAs. WT expression increased the total traction force by 40% compared with vinculin-null controls. This result demonstrates that vinculin enhances the transmission of traction forces. In contrast, V_H expression had no effect on the total traction force compared with null cells, showing that, despite localization to FAs, V_H by itself does not influence traction forces. T12-expressing cells exhibited twofold higher total traction forces than null cells, and the total traction force was 40% higher than that generated by WT-expressing cells. This result shows that disruption of vinculin head–tail inhibition enhances the transmission of traction forces. Blebbistatin reduced traction forces by 30% in WT- and T12-expressing cells, but the total traction force in null and V_H-expressing cells was insensitive to blebbistatin. This result shows that transmission of myosin contractility-dependent traction forces at FAs requires a full-length vinculin molecule containing both V_H and V_T.

We examined the relationship between cell area and traction force because Fu et al. (32) showed tight coupling between cell area and CSK tension, suggesting that cell area–traction force coupling represents a robust metric to analyze force responses to vinculin expression. Fig. 2*D* and Fig. S2*B* plot cell area and corresponding traction force for individual cells as well as regression lines. There is a strong correlation between cell area and traction force for null, WT-, and T12-expressing cells. Vinculin-null cells displayed a linear relationship between cell area and traction force, indicating that vinculin is dispensable for cell area–traction force coupling. This result supports a role for other FA components in the transmission of traction forces, such as direct talin–actin force transfer (33). However, WT expression significantly enhances coupling between cell area and traction force, as demonstrated by the twofold increase in the regression slope compared with null cells. T12 expression results in stronger coupling between cell area and traction force compared with WT, showing that vinculin head–tail inhibition plays a critical role in regulating traction forces. V_H-expressing cells showed no coupling between cell area and traction force. This result indicates that V_H disrupts basal cell area–traction force coupling, demonstrating that both V_H and V_T are required for vinculin-enhanced coupling between cell area and total traction force. Although blebbistatin reduces cell area and traction force, it

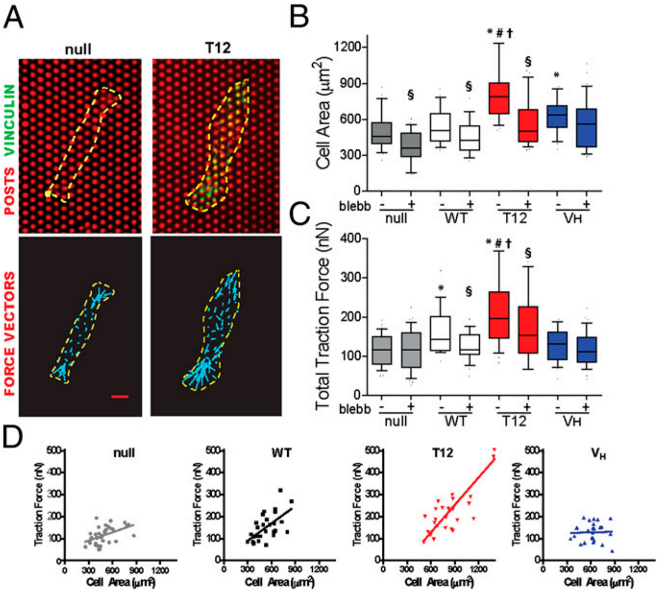

Fig. 2. Vinculin regulates traction forces. (*A*) Cells spread on mPADs (posts labeled red) showing localization of vinculin (eGFP) to FAs (*Upper*) and spreading (yellow outline) and force vectors (cyan arrows) (*Lower*). (Scale bar, 4 μm.) (*B*) Box-whisker plot (mean, 10th, 25th, 75th, and 90th percentile) for cell area (>24 cells per condition). Kruskal-Wallis $P < 0.0001$, $^{*}P < 0.05$ vs. null, $^{\#}P < 0.05$ vs. WT, $^{\dagger}P < 0.05$ vs. V_H; $^{\S}P < 0.05$ blebb vs. control. (*C*) Box-whisker plot (mean, 10th, 25th, 75th, and 90th percentile) for total traction force per cell (>24 cells). Kruskal-Wallis $P < 0.0001$, $^{*}P < 0.022$ vs. null, $^{\#}P < 0.01$ vs. WT, $^{\dagger}P < 0.01$ vs. V_H; $^{\S}P < 0.05$ blebb vs. control. (*D*) Relationship between traction force and cell area (>24 cells per condition) showing linear regression fits.

does not disrupt the relationship between cell area and traction force (Fig. S2C).

How Vinculin Head and Tail Domains and Autoinhibition Contribute to Adhesion Strength. We measured the steady-state (16 h after seeding) adhesion strength of cells expressing WT to FN using a spinning disk device. Whereas traction force measurements report on forces applied to the substrate arising from actomyosin contractility or actin polymerization, the adhesion strength assay measures the amount of force required to detach the cell from the ECM. The spinning disk exposes cells to a hydrodynamic shear force that increases linearly with radial position from the disk center and provides sensitive measurements of adhesion strength (Fig. S3*A*).

WT-expressing cells were cultured overnight on FN-coated micropatterned islands to eliminate differences in adhesive area and cell shape. This is an important consideration because expression of these constructs produces changes in cell area, a parameter that also regulates adhesion strength (6). Cells remained constrained to the micropatterned area as single cells. Expression of WT in vinculin-null MEF1 and MEF2 cells increased adhesion strength by 25% and 27%, respectively, over null controls (Fig. 3*A*). To test whether the increases in adhesion strength were caused by vinculin expression, we cultured WT-MEF2 cells in anhydrotetracycline to suppress expression. Under these conditions, the adhesion strength returned to the levels of null cells (Fig. 3*A*). Studies with blocking antibody demonstrated that adhesion to FN was mediated by β1 integrin (Fig. S3*B*). These results demonstrate that vinculin directly modulates adhesion strength and that this system provides direct measurements of β1 integrin–FN-mediated adhesion strength.

We next examined the adhesion strength of vinculin-null cells expressing vinculin mutants. V_H expression increased adhesion strength by 25% compared with null controls (Fig. 3*B*), indicating that recruitment of V_H to adhesive complexes increases adhesion strength independently from V_T. V_H increased adhesion strength to equivalent levels as WT. T12 expression increased adhesion strength by 50% over null cells (Fig. 3*B*), doubling the increase in adhesion strength by either WT or V_H. This result indicates that regulation of vinculin autoinhibition plays an important role in the generation of adhesion strength and that the active vinculin conformation presenting head and tail domains results in maximal adhesion strength.

We hypothesized that binding of V_H to talin or α-actinin was essential for vinculin-dependent increases in adhesion strength. We examined the effect of expressing a full-length, talin-/α-actinin-binding deficient mutant (A50I). No differences in adhesion strength were observed between A50I-expressing and null cells (Fig. S3*C*), indicating that vinculin binding to one or both of these ligands is essential for vinculin-mediated adhesion strength.

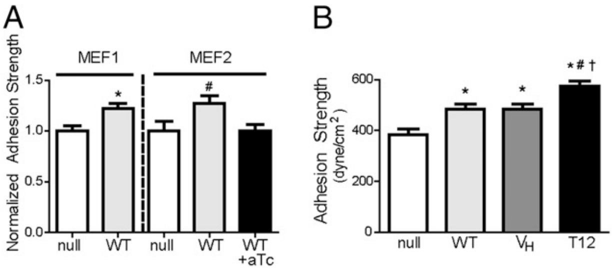

Fig. 3. Vinculin head and tail domains have distinct contributions to adhesion strength. (*A*) Expression of WT in vinculin-null cells increased adhesion strength over controls (**P* < 0.03 vs. null, #*P* < 0.05 vs. null, +aTc). aTc-induced suppression of WT expression returned adhesion strength to null levels. (*B*) V_H expression increased adhesion strength by 25%, whereas T12 increased adhesion strength by 50% compared with null controls. ANOVA *P* < 0.0001, **P* < 0.05 vs. null, #*P* < 0.05 vs. WT, and †*P* < 0.05 vs. V_H.

Physical Linkage Between Vinculin Head and Tail Domains Is Required for Maximal Adhesion Strength. We postulated that the increased adhesion strength for T12-expressing cells relative to V_H-expressing cells arises from differences in load transfer from the integrin–ECM complexes to the actin CSK via vinculin. We tested this model by independently expressing V_H and V_T in the same cell. We transiently transfected MEF1 cells with plasmids encoding for V_H, T12, or V_T or cotransfected plasmids for V_H and V_T. Transfected cells were enriched by flow cytometry sorting and seeded on FN islands. Image analysis demonstrated that vinculin mutants localized to FN patterns in a similar way as those in the stable lines (Fig. S4*A*). Cotransfected V_H and V_T localized to the FN island, but there was no strong colocalization because these two domains are not physically linked (Fig. S4*B*). Coexpression of separate V_H and V_T did not alter adhesion strength compared with expression of either domain, and adhesion strength was 25% lower than that for T12 expression (Fig. S4*C*). Expression of V_T resulted in similar levels of adhesion strength as V_H. This result was unexpected because V_T does not bind to the integrin–talin complex or α-actinin-rich lamellopodia protrusions (14, 34). A likely explanation for the effects of V_T is that this domain enhances adhesion strength by cross-linking actin to increase cortical CSK stiffness and load sharing among integrin bonds. Indeed, there is evidence that V_T enhances actin cross-linking and cortical CSK stiffness (29). These data show that the physical linkage between vinculin head and tail domains is required for maximal adhesion strength, indicating that force transfer from the adhesive clusters to the actin CSK via vinculin contributes to adhesion strength.

Vinculin Head–Tail Autoinhibition Regulates the Number of Integrin–FN Complexes and Recruitment of Vinculin and Talin. Because adhesion strength is regulated by the number/distribution of integrin–ECM complexes, FA assembly, and CSK interactions (6), we analyzed integrin binding and FA assembly to gain insights into possible reasons for the differences in adhesion strength. We first examined the effects of vinculin mutants on the levels and distribution of integrin–FN complexes using a cross-linking and detergent extraction method to selectively retain integrin–FN complexes. Fig. 4*A* presents images of single cells adhering to FN islands and immunostained for β1 integrin, and Fig. 4 *B* and *C* plot the fraction of the adhesive area occupied by integrin–FN complexes and the intensity of integrin staining over the micropatterned area. Vinculin-null cells assembled integrin β1–FN complexes along the periphery of the adhesive area, with minimal staining in the interior. WT expression did not change the spatial distribution or area occupied by integrin–FN complexes but resulted in a 15% increase in intensity. In contrast, V_H expression resulted in a fourfold increase in the area occupied by integrin–FN complexes, mostly localized to the periphery of the adhesive area, and a 40% increase in intensity compared with the null control. T12 expression yielded a fourfold increase in the area of integrin–FN complexes and a 50% increase in intensity compared with the null control. These results demonstrate that WT has a modest effect in regulating the number and spatial distribution of integrin–FN complexes and that presentation of V_H, either alone or in a mutant with disrupted head–tail binding, significantly increases the number and spatial distribution of integrin–FN complexes. Furthermore, the lack of differences in integrin–FN complexes between V_H and T12 indicates that V_T does not contribute significantly to the assembly or stability of integrin–FN complexes. These results indicate that vinculin head–tail inhibition to control exposure of V_H plays a major regulatory role in controlling the number and spatial distribution of ECM–integrin complexes.

We examined the role of vinculin autoinhibition on FA assembly by measuring recruitment of talin and the vinculin constructs to FAs. For all cells, talin and vinculin staining was

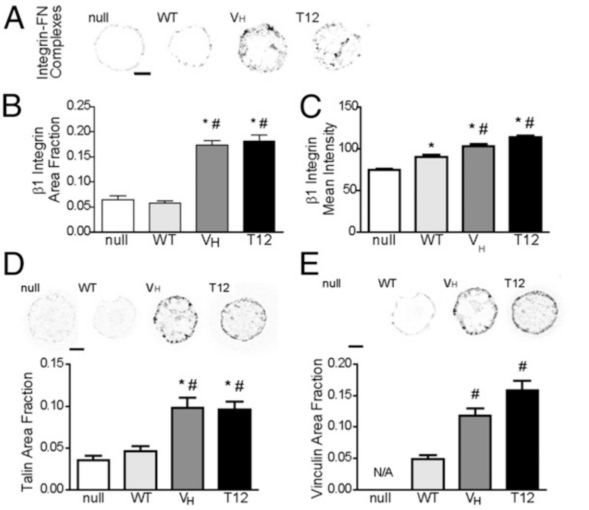

Fig. 4. Vinculin head–tail interaction regulates integrin–FN complexes and FA assembly. (*A*) Immunostaining for β1 integrin for cells adhering to FN micropatterned islands. Staining is shown as grayscale on white background to facilitate visualization. (Scale bar, 5 μm.) (*B*) Fraction of adhesive area occupied by integrin–FN complexes. ANOVA $P < 0.0001$, $^*P < 0.05$ vs. null, $^\#P < 0.05$ vs. WT. (*C*) Intensity of integrin staining over micropatterned area. ANOVA $P < 0.0001$, $^*P < 0.05$ vs. null, $^\#P < 0.05$ vs. WT (>60 cells per condition). (*D*) (*Upper*) Immunostaining for talin for cells adhering to FN islands. (Scale bar, 5 μm.) (*Lower*) Area of talin staining normalized to total adhesive area. ANOVA $P < 0.0001$, $^*P < 0.05$ vs. null, $^\#P < 0.05$ vs. WT. (*E*) (*Upper*) Immunostaining for vinculin for cells on FN islands (Scale bar, 5 μm.) (*Lower*) Area of vinculin staining normalized to total adhesive area. ANOVA $P < 0.0001$, $^*P < 0.05$ vs. null, $^\#P < 0.05$ vs. WT (>20 cells per condition).

restricted to the circumference of the micropatterned area (Fig. 4 *D* and *E*), consistent with the staining patterns for integrin–FN complexes. In addition to circumferential staining, T12- and V_H-expressing cells exhibited small vinculin and talin clusters in the interior of the adhesive area. Analysis of the adhesive area occupied by talin showed that WT expression had modest effects compared with null cells (Fig. 4*D*). In contrast, expression of V_H or T12 significantly enhanced the area occupied by talin and vinculin compared with WT and null cells (Fig. 4 *D* and *E*). These results demonstrate that WT has a modest effect in regulating FA assembly and that presentation of V_H, either alone or in a mutant with disrupted head–tail binding, significantly increases the area occupied by FAs. Furthermore, the lack of differences between V_H and T12 indicates that V_T does not contribute significantly to FA assembly. These results suggest that vinculin head–tail autoinhibition plays an important function in regulating FA assembly by controlling the exposure of V_H, resulting in an increase of both talin and vinculin recruitment to FAs.

Because there were no major differences in integrin–FN complexes and FA assembly between null and WT-expressing cells, we attribute the increased adhesion strength for WT to enhanced force distribution at the adhesive interface due to WT-mediated local cortical CSK stiffening and load transfer to the CSK. In contrast, the increased adhesion strength for V_H compared with the null control likely results from the higher number of integrin–FN complexes and enhanced FA assembly. Compared with V_H, T12 further increases adhesion strength without altering the levels of integrin–FN complexes or talin/vinculin recruitment to FAs. We attribute this additional increase in adhesion strength for T12 to V_T binding to the actin CSK to enhance load transfer.

Effect of Contractility on Adhesion Strength Is Mediated by Vinculin Autoinhibition. The increase in adhesion strength for T12 compared with V_H suggests that force transfer from FAs to the CSK via V_T is required for maximal adhesion strength. Because myosin contractility is critical to force generation (4, 5, 26, 35), we analyzed the contributions of myosin contractility to adhesion strength in the context of vinculin expression. Cells were seeded overnight on FN islands and exposed to blebbistatin (20 μM) for 30 min before measuring adhesion strength. Blebbistatin had no effect on adhesion strength for vinculin-null cells (Fig. 5). In contrast, blebbistatin reduced adhesion strength by 30% in WT-expressing cells. This result is consistent with our work demonstrating that vinculin is required for contractility-dependent adhesion strength (26). In this earlier study, we showed that the reductions in adhesion strength in response to contractility inhibition were associated with loss of vinculin and talin from FAs, in agreement with contractility-dependent FA assembly (36).

We hypothesized that the adhesion strength of V_H-expressing cells would be insensitive to blebbistatin treatment because this mutant cannot interact with the actin CSK because it lacks binding sites for Arp2/3, paxillin, and actin. Indeed, blebbistatin treatment had no effect on the adhesion strength of V_H-expressing cells (Fig. 5), indicating that the potential VASP-binding site in V_H is not capable of mediating interaction with actomyosin. Moreover, integrin–FN complex assembly and recruitment of talin and V_H to FAs were insensitive to blebbistatin (Fig. S5). This response differs from the effects of blebbistatin on WT vinculin-expressing cells and indicates that contractility-mediated changes in adhesion strength and FA assembly require a full-length, actin-binding vinculin molecule. We next analyzed the adhesion strength of T12-expressing cells with blebbistatin treatment. Surprisingly, blebbistatin enhanced adhesion strength for T12-expressing cells by 25% compared with untreated controls, in stark contrast to the effects of blebbistatin on WT-expressing cells (Fig. 5). Blebbistatin did not alter integrin–FN complex formation or vinculin and talin recruitment to FAs for T12-expressing cells (Fig. S5), so this enhancement in adhesion strength cannot be attributed to changes in integrin–FN bonds or FA assembly. These results indicate that vinculin autoinhibitory regulation is critical to contractility-mediated changes in adhesion strength, demonstrating a role for activated vinculin in force transfer. Furthermore, these data suggest that T12 promotes adhesion strength better than V_H through the ability of V_T to interact with the actin CSK and by the inability of T12 to substantially regain the autoinhibited conformation.

Vinculin Residence Times in FAs Correlate with Applied Force and Require Autoinhibitory Head–Tail Interactions. The striking difference in the effects of blebbistatin on the adhesion strength of WT- vs. T12-expressing cells implicates head–tail interactions in the regulation of contractility-mediated enhancements in adhesive force. We hypothesized that forces applied across vinculin maintain the molecule in its active conformation and counterbalance the high-affinity head–tail inhibition. For WT, inhibition of contractility unloads the vinculin molecule and promotes rebinding between V_H and V_T, resulting in vinculin inactivation and FA disassembly. For the T12 mutant, the head–tail interaction is reduced 100-fold, resulting in a molecule that, although not constitutively open (13), is much easier to open and harder to reclose. This mutant retains the WT affinity of V_H for talin and V_T for actin. Because of the ∼100-fold reduced head–tail autoinhibition,

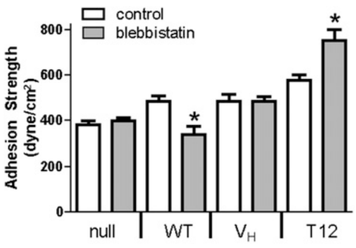

Fig. 5. Effect of contractility on adhesion strength is mediated by vinculin autoinhibition. $^*P < 0.05$ vs. control.

the T12 mutant would not reclose significantly when unloaded, and it would therefore transmit adhesive forces even during blebbistatin-mediated inhibition of contractility.

To test this model, we examined the relationship between vinculin residence times at FAs and applied force by performing fluorescence recovery after photobleaching (FRAP) experiments on cells on mPADs. We examined recovery times after photobleaching for eGFP-vinculin–containing FAs associated with posts with known deflections. In this fashion we could monitor vinculin dynamics at FAs under force. FRAP movies for WT-vinculin FAs under different traction forces are provided (Movies S1–S4), and Fig. S6*A* presents images of WT-containing FAs on mPADs before and after photobleaching. Fig. 6*A* displays FRAP recovery curves for WT in FAs transmitting different forces. The applied force remained constant over the 3-min FRAP experiment (Fig. S6 *B* and *C*). The half-life recovery time ($t_{1/2}$) vs. traction force for individual FAs in WT-expressing cells is plotted in Fig. 6*B*. Strikingly, we observed a linear relationship between applied force and recovery time for WT. A simple explanation for the strong correlation between vinculin residence time in FAs and applied force is that tension applied across the vinculin molecule maintains vinculin in the active conformation to increase its residence time in FAs. Blebbistatin (20 μM) eliminates the linear relationship between recovery time and force (Fig. 6*C*), consistent with our model. We also examined the recovery time vs. force relationship for cells expressing T12 and V_H (Fig. 6*D*). Both V_H and T12 exhibited twofold slower recovery times compared with WT, consistent with previous data (25, 31). However, in stark contrast to WT, recovery times for T12 and V_H did not correlate with applied forces at FAs. These results demonstrate that the vinculin head–tail interaction is critical to the coupling of vinculin residence time at FAs and applied force. Importantly, the lack of correlation of recovery times with force for V_H demonstrates that V_T is required for FA residence time–force coupling. Additionally, this result rules out the explanation that this phenomenon arises from force-mediated exposure of vinculin binding sites on talin (37). These findings support a mechanosensitive model for vinculin activation in which forces applied across vinculin maintain the molecule in its active conformation to increase residence times at FAs to transfer force.

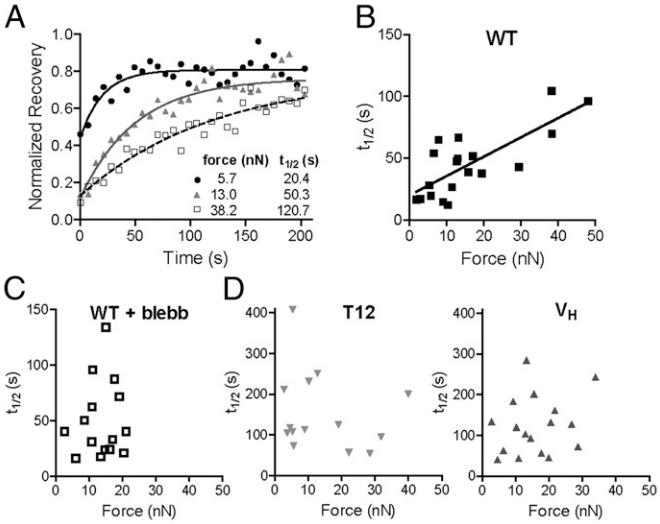

Fig. 6. Vinculin residence times in FAs correlate with applied force and require head–tail interactions. FRAP was performed on FAs on mPAD posts with known applied forces. (*A*) FRAP recovery curves for WT localized to FAs transmitting different forces. (*B*) Correlation between recovery time ($t_{1/2}$) and applied force (>15 cells analyzed per condition) for WT. Linear regression: $t_{1/2} = 1.56 \times \text{force} + 20.0$, $P < 0.0001$. (*C*) Blebbistatin treatment (20 μM) eliminates linear relationship between recovery time and force (no linear dependence, $P = 0.75$). (*D*) No correlation between $t_{1/2}$ and applied force was observed for T12 ($P = 0.45$) or V_H ($P = 0.35$). Different *y* axis scales were used between WT and V_H, T12 for ease of visualization.

Discussion

How vinculin and its interactions with binding partners transmit force remains poorly understood. Here we clearly demonstrate that vinculin regulates both traction forces and adhesion strength to ECM and dissect the contributions of different vinculin domains to these force outputs. The vinculin-dependent enhancements in traction force and adhesion strength quantify vinculin's contributions in force transmission and provide a mechanical basis to explain the effects of vinculin deletion on impaired cell spreading, migration, and muscle contraction. We show that vinculin regulates the coupling between cell area and traction force. The coupling between cell area and traction force reflects an integrated feedback response regulating cell shape and has been implicated in rigidity sensing (32). Our finding that full-length vinculin enhances cell area–traction force coupling but V_H completely disrupts this coupling indicates that vinculin is a key regulator of these mechanical responses and identifies a unique function for vinculin in mechanosensing.

Although V_H drives FA growth and V_T localizes to actin filaments (25), we demonstrate distinct contributions to force transmission for each domain. Vinculin transmits force by increasing ECM-bound integrin–talin complexes via V_H, whereas V_T transfers force to the actin CSK (Fig. S7). These mechanical functions require the talin/α-actinin-binding site on V_H. We note that vinculin-dependent changes in force transmission do not scale proportionally with changes in integrin-FN binding and FA assembly owing to biomechanical considerations, including spatial location of integrin–FN complexes and cortical CSK stiffness that result in nonlinear bond loading (6, 38). We also discovered an important role for vinculin's head–tail autoinhibitory interaction in regulating traction forces, adhesion strength, and the coupling between cell area and traction force. Finally, maximal adhesion strength requires V_H and V_T to be physically coupled, indicating that force transfer occurs through the vinculin molecule rather than independent contributions from each domain.

Although myosin contractility is critical to traction forces and adhesion strength, the contribution of vinculin to myosin contractility-dependent adhesive forces is unknown. We demonstrate that a full-length vinculin molecule containing both V_H and V_T is required for myosin contractility-dependent effects on traction force and adhesion strength, suggesting that force transfer occurs through the vinculin molecule. For WT-expressing cells, blebbistatin treatment reduced adhesion strength to vinculin-null levels, whereas blebbistatin did not alter adhesion strength in vinculin-null cells. Surprisingly, blebbistatin enhanced adhesion strength for T12-expressing cells, indicating that head–tail autoinhibition regulates the vinculin-dependent effects of myosin contractility on adhesion strength. One explanation for the blebbistatin-dependent increases in adhesion strength for T12 is that inhibition of contractility reduces the internal force applied to FAs, thereby increasing the force that can be supported by the external ECM–integrin linkage at FAs (39). The requirement for vinculin in myosin contractility-dependent adhesive forces establishes a unique function for vinculin in mechanotransduction beyond regulation of FA assembly (25, 28).

By applying FRAP to an FA under force, we discovered that vinculin residence time at an FA correlates linearly with the force applied to that FA. Vinculin residence time–force coupling requires a full-length molecule, head–tail autoinhibition, and myosin contractility. These results directly relate vinculin dynamics to force and complement studies showing that contractility influences FA dynamics (40). Our data support a model for vinculin stabilization in which forces applied across vinculin maintain the molecule in its active conformation to increase residence times at FAs to promote force transfer (Fig. S7). Direct measurements of the forces experienced by vinculin in the context of adhesion strength and traction forces are still needed to fully validate this model. Vinculin's binding partners and phosphorylation sites could provide indirect mechanisms for its force-regulated recruitment and activity.

Our findings support a mechanosensitive model for vinculin activation. Structural and biochemical data support a role for talin and actin binding in vinculin activation (13, 15, 41, 42). Given the requirements for the talin-binding site on V_H and the actin-binding V_T for force transmission, it is likely that coordinated activation by talin and actin provides a major mechanism driving vinculin activation and that force transmission across vinculin stabilizes its active conformation. This mechanism provides an explanation for the observation that vinculin recruitment to FAs is separable from mechanical loading (28). Force-dependent vinculin activation identifies another mechanism that complements mechanosensitive pathways at FAs, such as integrin–FN binding (43, 44) and talin stretching to expose binding sites (37).

The improved understanding of vinculin's contributions to force transmission provided by this work has several implications. First, vinculin regulates the transmission of adhesive forces by modulating ECM–integrin complexes via V_H and transmitting forces from these complexes to the actin CSK via V_T. Second, vinculin regulates cell area–traction force coupling and myosin contractility-dependent adhesion strength and traction forces. As such, vinculin likely provides "fine tuning" control required for coordinated processes like migration and contraction. Finally, force-based regulation of vinculin activation provides a mechanism to generate local mechanosensitive responses at FAs such as force-dependent FA growth (8, 36). Mechano-regulation of vinculin residence times at FAs represents a pathway for coordinated assembly of FAs at the leading edge and disassembly of FAs at the rear of the cell. In fact, experiments with a force sensor revealed high forces across vinculin at the leading edge and low forces at the trailing edge (28), consistent with our model. Collectively, this work provides these important insights into how vinculin's structure and binding partners interact with contractility to regulate force transmission.

Methods

Vinculin lines were generated by retroviral transduction of vinculin-null cells and FACS selection. Cell adhesion strength and traction forces were measured with a spinning disk device and mPADs, respectively. FRAP was performed on cells on mPADs. Detailed methods are presented in *SI Methods*.

ACKNOWLEDGMENTS. Funding was provided by National Institutes of Health Grants R01-GM065918 (to A.J.G.), R01-EB00262, R01-GM74048 (both to C.S.C.), and R01-GM41605 (to S.W.C.), RESBIO Technology Resource for Polymeric Biomaterials, Human Frontier Science Program Grant RGP0013 (to J.F.C.), and National Science Foundation Career Award DMR-0955811 (to J.E.C.) and CMMI-1129611 (to J.F.).

1. Hynes RO (2002) Integrins: Bidirectional, allosteric signaling machines. *Cell* 110(6): 673–687.
2. Wickström SA, Radovanac K, Fässler R (2011) Genetic analyses of integrin signaling. *Cold Spring Harb Perspect Biol* 3(2):a005116.
3. Beningo KA, Dembo M, Kaverina I, Small JV, Wang YL (2001) Nascent focal adhesions are responsible for the generation of strong propulsive forces in migrating fibroblasts. *J Cell Biol* 153(4):881–888.
4. Balaban NQ, et al. (2001) Force and focal adhesion assembly: A close relationship studied using elastic micropatterned substrates. *Nat Cell Biol* 3(5):466–472.
5. Tan JL, et al. (2003) Cells lying on a bed of microneedles: An approach to isolate mechanical force. *Proc Natl Acad Sci USA* 100(4):1484–1489.
6. Gallant ND, Michael KE, García AJ (2005) Cell adhesion strengthening: Contributions of adhesive area, integrin binding, and focal adhesion assembly. *Mol Biol Cell* 16(9): 4329–4340.
7. Kanchanawong P, et al. (2010) Nanoscale architecture of integrin-based cell adhesions. *Nature* 468(7323):580–584.
8. Riveline D, et al. (2001) Focal contacts as mechanosensors: externally applied local mechanical force induces growth of focal contacts by an mDia1-dependent and ROCK-independent mechanism. *J Cell Biol* 153(6):1175–1186.
9. Galbraith CG, Yamada KM, Sheetz MP (2002) The relationship between force and focal complex development. *J Cell Biol* 159(4):695–705.
10. Choquet D, Felsenfeld DP, Sheetz MP (1997) Extracellular matrix rigidity causes strengthening of integrin-cytoskeleton linkages. *Cell* 88(1):39–48.
11. Smilenov LB, Mikhailov A, Pelham RJ, Marcantonio EE, Gundersen GG (1999) Focal adhesion motility revealed in stationary fibroblasts. *Science* 286(5442):1172–1174.
12. Ziegler WH, Liddington RC, Critchley DR (2006) The structure and regulation of vinculin. *Trends Cell Biol* 16(9):453–460.
13. Cohen DM, Chen H, Johnson RP, Choudhury B, Craig SW (2005) Two distinct head-tail interfaces cooperate to suppress activation of vinculin by talin. *J Biol Chem* 280(17): 17109–17117.
14. Johnson RP, Craig SW (1995) F-actin binding site masked by the intramolecular association of vinculin head and tail domains. *Nature* 373(6511):261–264.
15. Chen H, Choudhury DM, Craig SW (2006) Coincidence of actin filaments and talin is required to activate vinculin. *J Biol Chem* 281(52):40389–40398.
16. Peng X, Maiers JL, Choudhury D, Craig SW, DeMali KA (2012) α-Catenin uses a novel mechanism to activate vinculin. *J Biol Chem* 287(10):7728–7737.
17. Chen H, Cohen DM, Choudhury DM, Kioka N, Craig SW (2005) Spatial distribution and functional significance of activated vinculin in living cells. *J Cell Biol* 169(3):459–470.
18. Horwitz AF, Duggan K, Buck CA, Beckerle MC, Burridge K (1986) Interaction of plasma membrane fibronectin receptor with talin—a transmembrane linkage. *Nature* 320(6062):531–533.
19. Ohmori T, et al. (2010) Vinculin activates inside-out signaling of integrin αIIbβ3 in Chinese hamster ovary cells. *Biochem Biophys Res Commun* 400(3):323–328.
20. Zemljic-Harpf AE, et al. (2007) Cardiac-myocyte-specific excision of the vinculin gene disrupts cellular junctions, causing sudden death or dilated cardiomyopathy. *Mol Cell Biol* 27(21):7522–7537.
21. Huang Y, Zhang W, Gunst SJ (2011) Activation of vinculin induced by cholinergic stimulation regulates contraction of tracheal smooth muscle tissue. *J Biol Chem* 286(5):3630–3644.
22. Barstead RJ, Waterston RH (1991) Vinculin is essential for muscle function in the nematode. *J Cell Biol* 114(4):715–724.
23. Xu W, Baribault H, Adamson ED (1998) Vinculin knockout results in heart and brain defects during embryonic development. *Development* 125(2):327–337.
24. Xu W, Coll JL, Adamson ED (1998) Rescue of the mutant phenotype by reexpression of full-length vinculin in null F9 cells; effects on cell locomotion by domain deleted vinculin. *J Cell Sci* 111(Pt 11):1535–1544.
25. Humphries JD, et al. (2007) Vinculin controls focal adhesion formation by direct interactions with talin and actin. *J Cell Biol* 179(5):1043–1057.
26. Dumbauld DW, et al. (2010) Contractility modulates cell adhesion strengthening through focal adhesion kinase and assembly of vinculin-containing focal adhesions. *J Cell Physiol* 223(3):746–756.
27. Diez G, Auernheimer V, Fabry B, Goldmann WH (2011) Head/tail interaction of vinculin influences cell mechanical behavior. *Biochem Biophys Res Commun* 406(1): 85–88.
28. Grashoff C, et al. (2010) Measuring mechanical tension across vinculin reveals regulation of focal adhesion dynamics. *Nature* 466(7303):263–266.
29. Mierke CT, et al. (2008) Mechano-coupling and regulation of contractility by the vinculin tail domain. *Biophys J* 94(2):661–670.
30. DeMali KA, Barlow CA, Burridge K (2002) Recruitment of the Arp2/3 complex to vinculin: Coupling membrane protrusion to matrix adhesion. *J Cell Biol* 159(5): 881–891.
31. Cohen DM, Kutscher B, Chen H, Murphy DB, Craig SW (2006) A conformational switch in vinculin drives formation and dynamics of a talin-vinculin complex at focal adhesions. *J Biol Chem* 281(23):16006–16015.
32. Fu J, et al. (2010) Mechanical regulation of cell function with geometrically modulated elastomeric substrates. *Nat Methods* 7(9):733–736.
33. Jiang G, Giannone G, Critchley DR, Fukumoto E, Sheetz MP (2003) Two-piconewton slip bond between fibronectin and the cytoskeleton depends on talin. *Nature* 424(6946): 334–337.
34. Menkel AR, et al. (1994) Characterization of an F-actin-binding domain in the cytoskeletal protein vinculin. *J Cell Biol* 126(5):1231–1240.
35. Gardel ML, et al. (2008) Traction stress in focal adhesions correlates biphasically with actin retrograde flow speed. *J Cell Biol* 183(6):999–1005.
36. Chrzanowska-Wodnicka M, Burridge K (1996) Rho-stimulated contractility drives the formation of stress fibers and focal adhesions. *J Cell Biol* 133(6):1403–1415.
37. del Rio A, et al. (2009) Stretching single talin rod molecules activates vinculin binding. *Science* 323(5914):638–641.
38. Evans EA (1985) Detailed mechanics of membrane-membrane adhesion and separation. II. Discrete kinetically trapped molecular cross-bridges. *Biophys J* 48(1): 185–192.
39. Coyer SR, et al. (2012) Nanopatterning reveals an ECM area threshold for focal adhesion assembly and force transmission that is regulated by integrin activation and cytoskeleton tension. *J Cell Sci* 125(Pt 21):5110–5123.
40. Wolfenson H, Bershadsky A, Henis YI, Geiger B (2011) Actomyosin-generated tension controls the molecular kinetics of focal adhesions. *J Cell Sci* 124(9):1425–1432.
41. Izard T, et al. (2004) Vinculin activation by talin through helical bundle conversion. *Nature* 427(6970):171–175.
42. Bakolitsa C, et al. (2004) Structural basis for vinculin activation at sites of cell adhesion. *Nature* 430(6999):583–586.
43. Friedland JC, Lee MH, Boettiger D (2009) Mechanically activated integrin switch controls alpha5beta1 function. *Science* 323(5914):642–644.
44. Kong F, García AJ, Mould AP, Humphries MJ, Zhu C (2009) Demonstration of catch bonds between an integrin and its ligand. *J Cell Biol* 185(7):1275–1284.

Supporting Information

Dumbauld et al. 10.1073/pnas.1216209110

SI Methods

Cells and Reagents. Vinculin-null mouse embryonic fibroblasts (MEF1 and MEF2) were a kind gift from Eileen Adamson (Burnham Institute, La Jolla, CA). Monoclonal antibodies against vinculin (V284; Millipore) and talin (8d4; Sigma) were used for immunostaining and Western blotting. Monoclonal antibody against extracellular domain of β1 integrin (9EG7; Millipore) was used for integrin binding study. Polyclonal antibody against β1 integrin (ab1950; Chemicon) was used for adhesion blocking study. Poly(dimethylsiloxane) (PDMS) elastomers and curing agents were obtained from Dow Corning. Dithiobis(sulfosuccinimidylpropionate) (DTSSP) was purchased from Pierce Chemical. Tri(ethylene glycol)-terminated alkanethiol $[HO(CH_2CH_2O)_3\text{-}(CH_2)_{11}SH]$ was purchased from ProChimia Surfaces. All other reagents including hexadecanethiol $[H_3C(CH_2)_{15}SH]$ were purchased from Sigma. Human plasma fibronectin was purchased from Invitrogen. Vinculin head (V_H)-CFP and vinT-YFP constructs were a kind gift from Christoph Ballestrem (University of Manchester, United Kingdom).

Retroviral Vectors for Enhanced GFP-Vinculin Expression and Transduction. Retroviral plasmids pTJ66-tTA and pXF40 were previously described (1) (Fig. S1). enhanced green fluorescent protein (pEGFP)-C1 WT, T12, V_H vinculin plasmids have been described (2–5). One AgeI restriction site was inserted into the multiple cloning site of pXF40, the retroviral expression vector. The oligonucleotides 5′-AGCTTGTCAGCTACCGGTGCTACTGCA-3′ and 5′-AGCTTGCAGTAGCACCGGTAGCTGACA-3′ were annealed together, creating HindIII-compatible overhangs at each end. This product was then ligated into a linearized pXF40 vector that had been digested with HindIII. Finally, the enhanced GFP (eGFP)-vinculin constructs were digested from pEGFP-C1 with AgeI and SalI and ligated into the SalI and AgeI-digested pXF40 vector. The pXF40-eGFP-vinculin vectors transcribe the eGFP-vinculin gene from the tetracycline-inducible promoter. All vectors were verified by sequencing the ligation points.

Retroviral stocks were produced by transient transfection of helper virus-free Phoenix amphotropic producer cells with plasmid DNA (6). Vinculin-null MEFs were cultured and plated on tissue culture polystyrene at 2×10^4 cells/cm^2 24 h before retroviral transduction. Cells were transduced with 0.2 mL/cm^2 of equal parts pTJ66-tTA and pXF40-eGFP-vinculin retroviral supernatant supplemented with 4 μg/mL hexadimethrine bromide (Polybrene) and 10% FBS, and centrifuged at $1,200 \times g$ for 30 min in a swinging bucket rotor. Retroviral supernatant was replaced with growth media [DMEM, 10% (vol/vol) FBS, 100 U/mL penicillin G sodium, 100 μg/mL streptomycin sulfate, 1% nonessential amino acids, and 1% sodium pyruvate]. Five days after transduction, eGFP-expressing cells were FACS sorted, expanded, and either used for experimentation or cryopreserved. Expression of vinculin constructs was verified by Western blot and immunofluorescence microscopy.

Traction Force Measurements. Microfabricated postarray deflection device (mPAD) silicon masters were prepared as previously described (7). The elastomeric micropost arrays were fabricated using PDMS replica molding. To make a microfabricated post array template, PDMS prepolymer was cast on top of mPAD silicon masters, cured at 110 °C for 1 h, peeled off, oxidized with oxygen plasma (Plasma-Preen; Terra Universal), and silanized with (tridecafluoro-1,1,2,2,-tetrahydrooctyl)-1-trichlorosilane vapor overnight under vacuum. To make the final PDMS mPAD device, PDMS prepolymer was cast on the template, degassed under vacuum, and cured at 110 °C for 20 h and peeled off the template. Peeling-induced collapse of the mPADs was rectified by sonication in 100% ethanol, followed by supercritical drying in liquid CO_2 using a critical point dryer (Samdri-PVT-3D; Tousimis).

Flat PDMS stamps were generated by casting PDMS prepolymer on silanized silicon wafers. Stamps were coated in saturating concentration of fibronectin (FN) (50 μg/mL in PBS) for 1 h. These stamps were washed in distilled water and dried under a stream of N_2. FN-coated stamps were placed in contact with surface-oxidized mPAD substrates (UVO-Model 342; Jelight). mPAD substrates were labeled with 5 μg/mL of Δ^9-DiI (Invitrogen) in distilled water for 1 h. mPAD substrates were then transferred to a solution of 0.1% Pluronics F127 (Sigma-Aldrich) to prevent nonspecific protein absorption. WT, V_H, T12, and null eGFP-vinculin MEF cells were seeded in growth medium and then allowed to spread overnight.

mPAD substrates were transferred to an aluminum coverslip holder (Attoflour Cell Chamber; Invitrogen) for live cell microscopy and placed in a stage top incubator that regulated temperature, humidity, and CO_2 (Live Cell; Pathology Devices). Confocal images were taken with a Nikon A1-Confocal Module connected to a Nikon TE-300 inverted microscope using a high magnification objective (CFI Plan Apochromat total internal reflection fluorescence (TIRF) 60× oil, N.A. 1.45; Nikon). Post images were captured using a 590-nm laser, and vinculin images were captured using a 488-nm laser. For force measurements, the top and bottom of the posts were sequentially imaged and the deflection measured. The resulting force, F, was calculated using Euler-Bernoulli beam theory where

$$F = \delta \frac{3\pi E D^4}{64 L^3},$$

in which E, D, L, and δ are the Young's modulus, post diameter, post height, and post deflection. We analyzed >50 posts per condition.

Micropatterned Substrates. Micropatterned substrates were generated by microcontact printing of self-assembled monolayers of alkanethiols on gold (8). Arrays of CH_3-terminated alkanethiol circles were stamped on to Au-coated glass coverslips using a PDMS stamp. The remaining exposed areas were functionalized with a tri(ethylene glycol)-terminated alkanethiol. Patterned substrates were coated with FN (2.0 μg/mL) and blocked with 1% heat-denatured BSA. This process results in an array of FN-coated circular islands 15 μm in diameter spaced 75 μm apart to promote single cell attachment to each island.

Adhesion Strength Assay. Adhesion strength was measured using our spinning disk system (8–10). Micropatterned substrates with adherent cells were spun in PBS + 2 mM dextrose for 5 min at constant speed. The applied shear stress (τ) is given by the formula

$$\tau = 0.8r\sqrt{\rho\mu\omega^3},$$

where r is the radial position from the center of the patterned coverslip, and ρ, μ, and ω are the fluid density, viscosity, and rotational speed, respectively. In some experiments the spinning buffer was supplemented with 5% dextran to increase the fluid viscosity. After spinning, cells were fixed in 3.7% formaldehyde, permeabilized in 1% Triton X-100, stained with ethidium homodimer-1 (Invitrogen), and counted at specific radial positions using a 10× objective lens in a Nikon TE300 microscope equipped with a Ludl motorized stage, Spot-RT camera, and Image-Pro-6.3 analysis system. A total of 61 fields (80–100 cells per field before spinning) were analyzed, and cell counts were normalized to the number of cells in the center of the disk. The fraction of adherent cells (f) was then fitted to a sigmoid curve

$$f = \frac{1}{(1 + e^{[b(\tau - \tau_{50})]})},$$

where τ_{50} is the shear stress for 50% detachment, and b is the inflection slope. τ_{50} characterizes the mean adhesion strength for a population of cells.

Immunostaining for Integrin–FN Complexes and Focal Adhesions. Integrin binding was quantified via a cross-linking/extraction procedure (11, 12). After rinsing cultures three times with PBS, DTSSP (1.0 mM in cold PBS + 2 mM dextrose) was incubated for 30 min to cross-link integrins to their bound ligands. The cross-linking reaction was quenched by addition of Tris (50 mM in PBS) for 15 min. Uncross-linked cellular components were then extracted in 0.1% SDS containing 10 μg/mL leupeptin, 10 μg/mL aprotinin, and 350 μg/mL PMSF. Integrins cross-linked to their bound ligands were visualized by immunostaining with β_1 integrin-specific monoclonal antibody 9EG7. Integrin area fractions were quantified using a custom MATLAB image analysis script. Briefly, original images were first background subtracted. A threshold intensity mask was applied, and pixels above the specified intensity threshold were considered positive for integrin staining.

For staining of focal adhesion (FA) components, cells were permeabilized in CSK-stabilizing buffer [(0.5% Triton X-100: 10 mM Pipes buffer, 50 mM NaCl, 150 mM sucrose, 3mM $MgCl_2$, 0.5% (vol/vol) Triton X-100, 1 mM PMSF, 1 μg/mL leupeptin, 1 μg/mL aprotinin, and 1 μg/mL pepstatin] for 10 min, fixed in 3.7% formaldehyde for 5 min, blocked in 5% goat serum, and incubated with primary antibodies against FA components followed by AlexaFluor-labeled secondary antibodies (Invitrogen). Images were captured using a Nikon Eclipse E400 equipped with a 60× APO (1.49 N.A.) TIRF objective and Spot RT Camera/Software. Focal adhesion area fractions were quantified using a custom MATLAB image analysis script. Briefly, original images of immunostained cells were first background subtracted and then pixel intensity thresholded to determine FA area.

Fluorescence Recovery After Photobleaching. A confocal microscope head (Nikon C1) and inverted microscope (Nikon TE 300) equipped with a Coherent Sapphire solid-state 488 laser under the control of Nikon EZ-C1 software were used for FRAP experiments. Cells were seeded overnight on FN-coated mPADs. Cell-seeded mPADs were loaded into an Attofluor cell chamber (Invitrogen) and allow to equilibrate for >20 min. A 60× APO TIRF (1.49 N.A.) objective (Nikon) was used for imaging. Initial fluorescence intensity was measured using low laser power (1.5–2.5%) followed by photobleaching of a 0.85-μm-diameter circle inside FAs at 10% laser power for 1 zoomed pass (bleached circle is defined within 256 × 256 pixel box). The recovery of fluorescence was monitored every 7 s (10 s for V_H and T12) until a plateau in recovery was reached (5 prebleach and 30 postbleach images were acquired in each series recorded). Image series were imported into MATLAB, where background subtraction and correction for incidental bleaching during image acquisition were applied to data extracted from the bleached region. Curves were fit to single exponential recovery model by assuming a reaction-dominated system and disregarding any effects of diffusion, and the characteristic recovery time ($t_{1/2}$) was calculated as previously described (2).

Transient Transfection of Vinculin Constructs. MEF1 cells were transfected using a Nucleofector II (Amaxa). For each sample, 2 million cells were resuspended in 100 μL of nucleofector solution MEF2 with 2.5 μg of plasmid DNA coding for indicated vinculin-eGFP construct. Plasmid-containing cell suspension was loaded into the Nucleofector cuvette and transfected with program T-20. Immediately after transfection, cells were transferred to a 1.5-mL centrifuge tube containing 500 μL of prewarmed RPMI 1640 (Invitrogen) and incubated for 15 min to minimize cell death. Cells were then transferred into 100-mL plates containing normal growth media (DMEM, 10% FBS, 1% sodium pyruvate, 1% penicillin-streptomycin, and 1% nonessential amino acids). Cells were sorted 72 h after transfection for eGFP expression and seeded onto micropatterned surfaces. The next day the spinning disk assay and immunostaining were performed.

Western Blotting. Cells were washed with PBS and lysed in cold radioimmunoprecipitation assay buffer [1% Triton X-100, 1% sodium deoxycholate, 0.1% SDS, 150 mM NaCl, 150 mM Tris-HCl (pH 7.2), 350 μg/mL phenylmethylsulfonyl fluoride, 10 μg/mL leupeptin, 10 μg/mL aprotinin, and 1 mM sodium orthovanadate] for 20 min. Lysates were pipette up and down ~25 times to shear the DNA and then clarified by centrifugation at 10,000 × g for 10 min. Protein concentration was then determined using a Micro BCA protein assay kit (Pierce). Equal amounts of protein (25 μg) were boiled in Laemmli sample buffer [2% SDS, 10% glycerol, 100 mM DTT, 60 mM Tris·HCl (pH 6.8), and 0.001% bromophenol blue] for 10 min and separated by SDS/PAGE. Proteins were transferred by electrophoresis onto nitrocellulose membranes and blocked with Blotto (5% nonfat dry milk, 0.02% sodium azide, and 0.2% Tween 20 in PBS without Ca^{2+} /Mg^{2+}) overnight at 4 °C. Membranes were incubated with appropriate antibodies in Blotto for 1 h at room temperature under gentle rocking. Membranes were washed in TBS-Tween [20 mM Tris·HCl (pH 7.6), 137 mM NaCl, and 0.1% Tween 20) for 30 min and incubated in near-infrared conjugated-secondary antibodies (LiCor Biosciences) for 30 min followed by 30 min washing in TBS-Tween. Membranes were imaged with a LiCor Odyssey Imager (LiCor Biosciences).

Statistical Analysis. Data are presented as mean ± SEM. Regression analyses were performed using SigmaPlot 2001 software (SPSS). ANOVA, Kruskal-Wallis nonparametric tests, and post hoc tests were performed in GraphPad Prism.

1. Gersbach CA, Le Doux JM, Guldberg RE, García AJ (2006) Inducible regulation of Runx2-stimulated osteogenesis. *Gene Ther* 13(11):873–882.
2. Cohen DM, Kutscher B, Chen H, Murphy DB, Craig SW (2006) A conformational switch in vinculin drives formation and dynamics of a talin-vinculin complex at focal adhesions. *J Biol Chem* 281(23):16006–16015.
3. Chen H, Choudhury DM, Craig SW (2006) Coincidence of actin filaments and talin is required to activate vinculin. *J Biol Chem* 281(52):40389–40398.
4. Cohen DM, Chen H, Johnson RP, Choudhury B, Craig SW (2005) Two distinct head-tail interfaces cooperate to suppress activation of vinculin by talin. *J Biol Chem* 280(17): 17109–17117.
5. Chen H, Cohen DM, Choudhury DM, Kioka N, Craig SW (2005) Spatial distribution and functional significance of activated vinculin in living cells. *J Cell Biol* 169(3):459–470.
6. Byers BA, Pavlath GK, Murphy TJ, Karsenty G, García AJ (2002) Cell-type-dependent up-regulation of in vitro mineralization after overexpression of the osteoblast-specific transcription factor Runx2/Cbfal. *J Bone Miner Res* 17(11):1931–1944.
7. Fu J, et al. (2010) Mechanical regulation of cell function with geometrically modulated elastomeric substrates. *Nat Methods* 7(9):733–736.
8. Gallant ND, Michael KE, García AJ (2005) Cell adhesion strengthening: Contributions of adhesive area, integrin binding, and focal adhesion assembly. *Mol Biol Cell* 16(9): 4329–4340.

9. García AJ, Ducheyne P, Boettiger D (1997) Quantification of cell adhesion using a spinning disc device and application to surface-reactive materials. *Biomaterials* 18(16): 1091–1098.

10. García AJ, Huber F, Boettiger D (1998) Force required to break alpha5beta1 integrin-fibronectin bonds in intact adherent cells is sensitive to integrin activation state. *J Biol Chem* 273(18):10988–10993.

11. García AJ, Vega MD, Boettiger D (1999) Modulation of cell proliferation and differentiation through substrate-dependent changes in fibronectin conformation. *Mol Biol Cell* 10(3):785–798.

12. Keselowsky BG, García AJ (2005) Quantitative methods for analysis of integrin binding and focal adhesion formation on biomaterial surfaces. *Biomaterials* 26(4): 413–418.

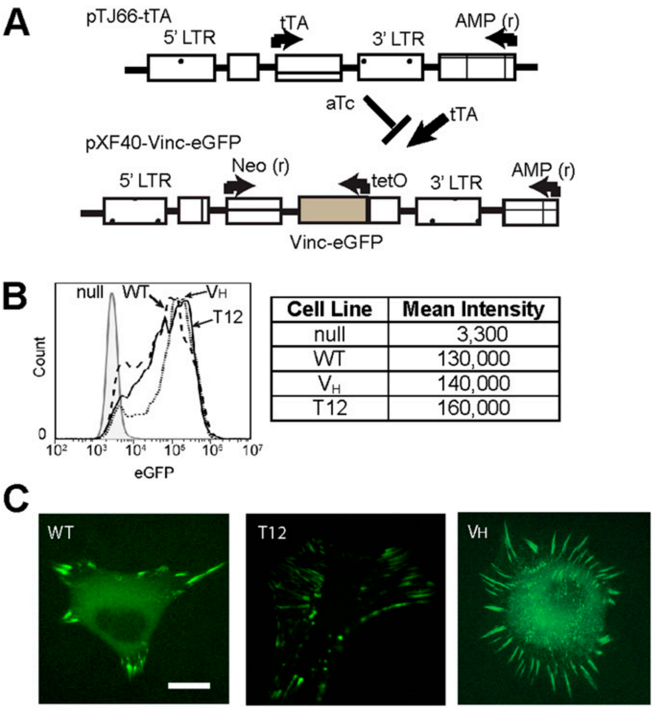

Cell Line	Mean Intensity
null	3,300
WT	130,000
V_H	140,000
T12	160,000

Fig. S1. Vinculin variant-expressing cell lines. (*A*) Maps of expression vectors. (*B*) Expression levels for vinculin variants in cell lines as determined by flow cytometry for eGFP. (*C*) Vinculin location to FAs in MEF1 cells expressing V_H and T12. (Scale bar, 10 μm.)

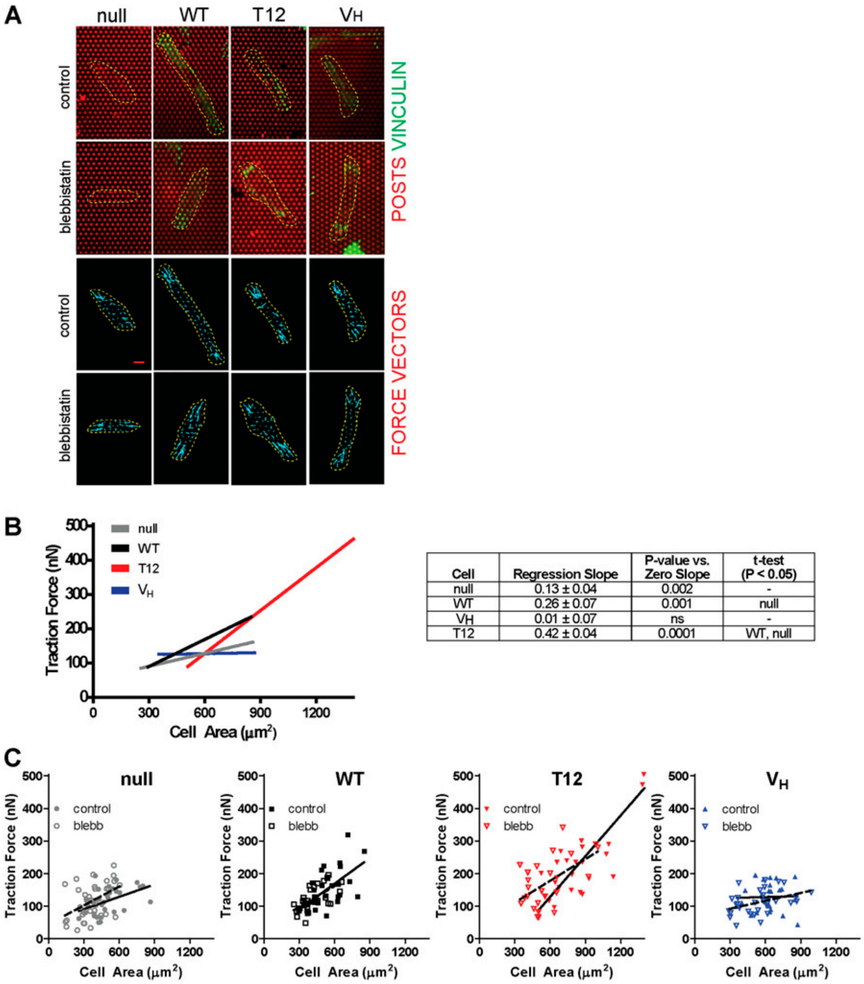

Cell	Regression Slope	P-value vs. Zero Slope	t-test (P < 0.05)
null	0.13 ± 0.04	0.002	-
WT	0.26 ± 0.07	0.001	null
VH	0.01 ± 0.07	ns	-
T12	0.42 ± 0.04	0.0001	WT, null

Fig. S2. Traction forces for vinculin-expressing cell lines in the presence or absence of blebbistatin (20 μM). (*A*) (*Upper*) Fluorescence images for FN-coated posts (red) and eGFP-vinculin (green), with cell outlined in yellow. (*Lower*) Calculated force vectors. (*B*) Linear regression fits (lines) and parameters (table, mean ± SEM) demonstrating significant differences among vinculin variants. (*C*) Plots of traction force vs. cell area for vinculin mutants, demonstrating that blebbistatin treatment does not disrupt traction force–cell area coupling. Linear fits shown as solid (control) and dashed (blebbistatin) lines.

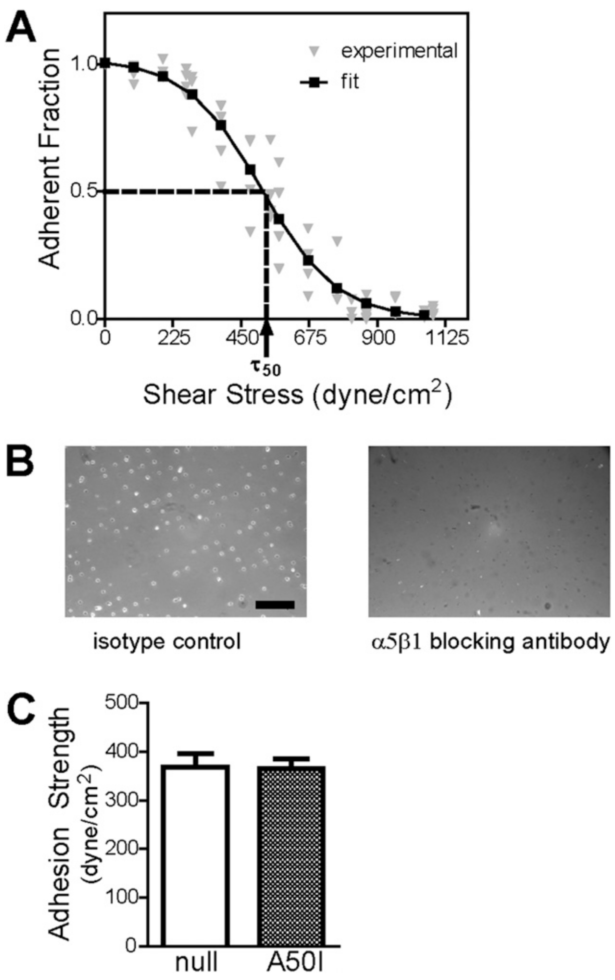

isotype control

α5β1 blocking antibody

Fig. S3. Cell adhesion strength for vinculin-expressing cell lines. (*A*) Cell detachment profile showing fraction of adherent cells (f) as a function of shear stress (τ) for a single experiment. Experimental cell counts (gray triangles) are fit to a sigmoid (line, black square) to obtain the shear stress for 50% detachment (τ50), which represents the mean adhesive strength. For the experiment shown (T12), the adhesion strength is 516 dyne/cm^2 (R^2 = 0.95). (*B*) Adhesion of MEFs on FN coated substrates is $\alpha_5\beta_1$ integrin specific. Cells were trypsinized from dish, quenched in serum containing media, pelleted, and resuspended in appropriate antibody for 15 min with shaking. Blocking $\alpha_5\beta_1$ integrin binding to fibronectin-coated islands eliminated cell attachment to micropatterned islands compared with isotype control. (Scale bar, 200 μm.) (*C*) No differences in adhesion strength (mean ± SEM) were observed upon expression of full-length, talin-binding deficient mutant A50I.

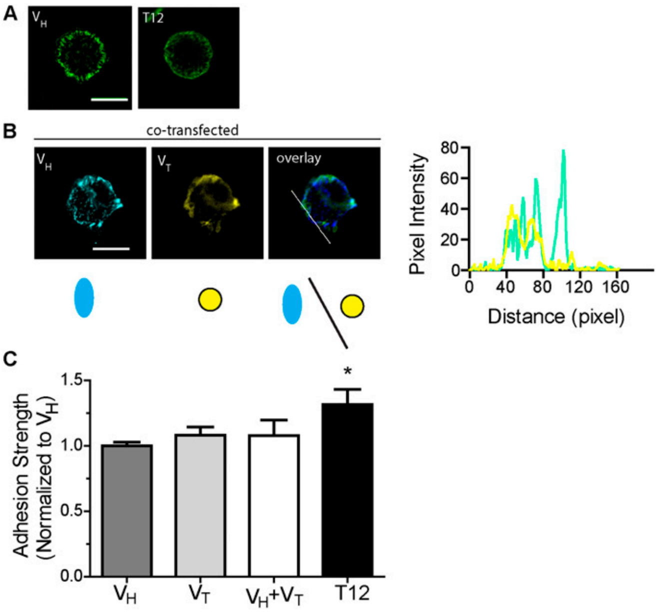

Fig. S4. Physical linkage between the head and tail domains of vinculin is required for maximal adhesion strength. (*A*) V_H and T12 constructs transiently transfected into vinculin-null cells and seeded on micropatterned islands revealed vinculin localization patterns consistent with previous results using retroviral expression of vinculin constructs. (Scale bar, 10 μm.) (*B*) Expression plasmids encoding V_H (V_H-CFP) and V_T (V_T-YFP) were cotransfected into MEF1 cells and seeded on micropatterned islands. (Scale bar, 10 μm.) Cartoon representation of the lack of physical connection between V_H and V_T. Line profile of V_H-CFP and V_T-YFP overlay demonstrates that V_T does not strongly colocalize with FA-associated V_H. (*C*) Adhesion strength (mean ± SEM) of indicated constructs transfected into vinculin-null cells. ANOVA $P < 0.02$, *$P < 0.05$ vs. all groups.

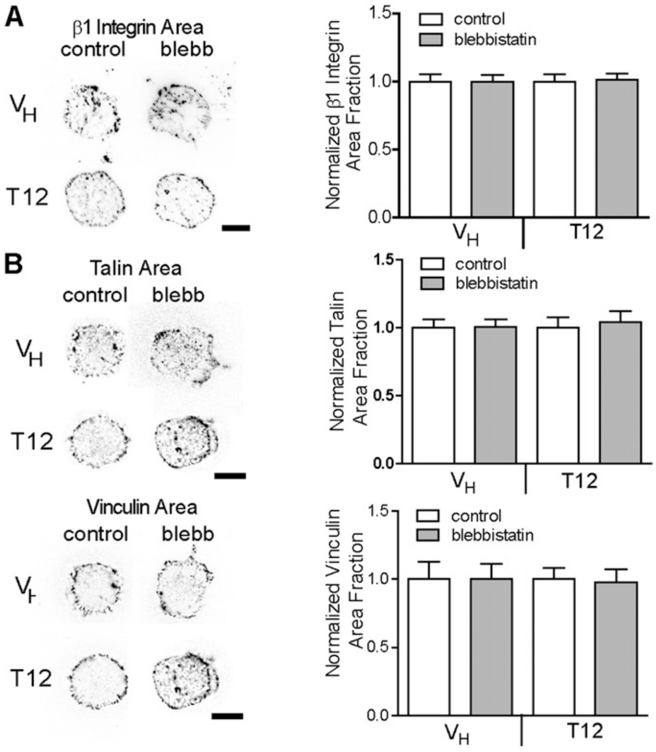

Fig. S5. Effects of blebbistatin treatment on integrin–FN complexes and focal adhesion assembly. (*A*) Immunostaining for β1 integrin in cells adhering to FN islands in the presence or absence of blebbistatin (20 μM). (Scale bar, 5 μm.) Staining is shown as grayscale on white background. Bar graph shows fraction of adhesive area occupied by integrin–FN complexes, normalized to untreated control. (*B*) Immunostaining for talin (*Upper*) and vinculin (*Lower*) in vinculin cell lines adhering to FN islands in the presence or absence of blebbistatin (20 μM). Staining is shown as grayscale on white background. Graphs present fraction of adhesive area occupied by talin and vinculin.

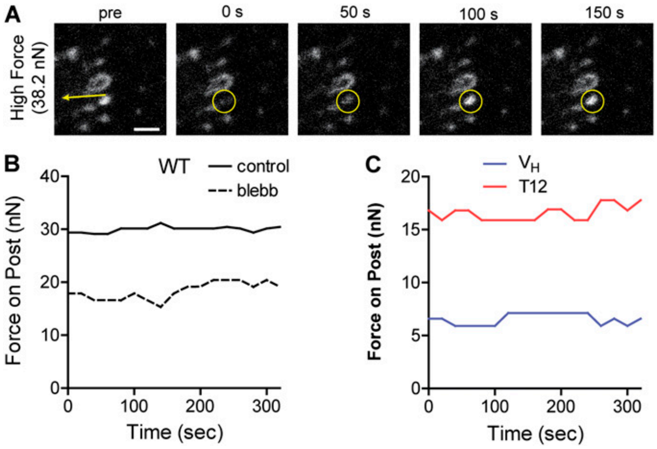

Fig. S6. Vinculin residence time at FAs depends on applied force. FRAP was performed on FAs on mPAD posts with known applied forces. (*A*) Time frames of WT-containing FA on mPADs before and after photobleaching. The yellow arrow in the prephotobleaching frame indicates the direction and magnitude of applied force, and the photobleached FA is marked with a yellow circle. (Scale bar, 4 μm.) (*B*) Force traces during FRAP experiment for WT-expressing cells in the presence and absence of blebbistatin showing constant force at FAs. (*C*) Force traces during FRAP experiment for T12- and V_H-expressing cells showing constant force at FAs.

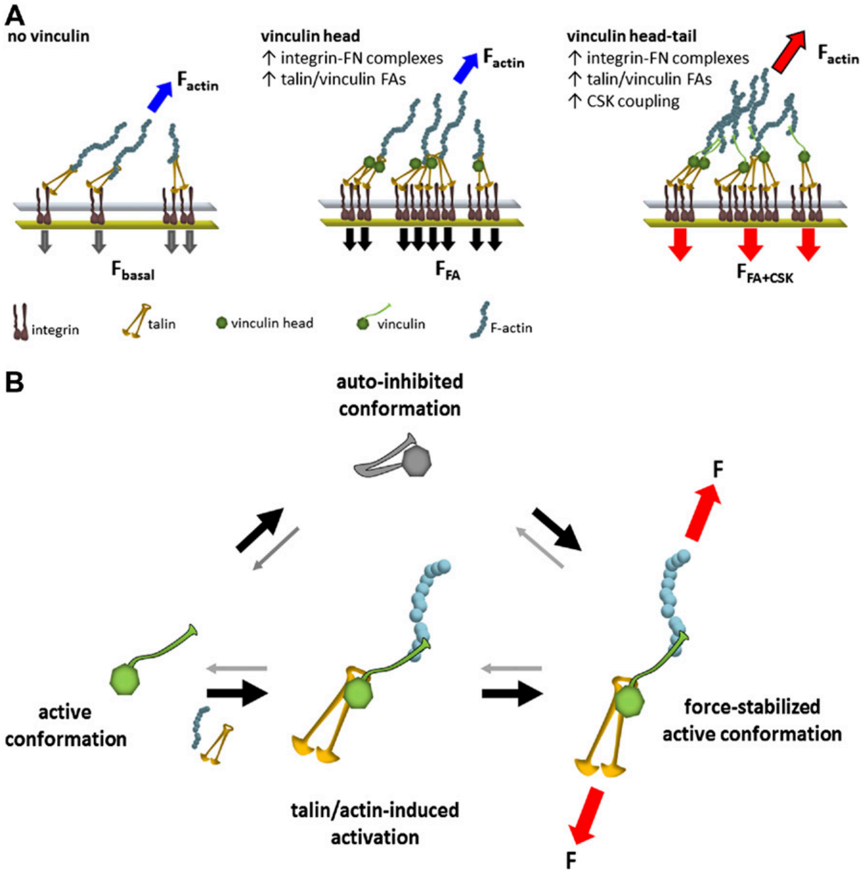

Fig. S7. Model for vinculin regulation of adhesive forces. (*A*) Vinculin differentially regulates adhesive forces. In the absence of vinculin, basal levels of adhesive forces (F_{basal}) and cytoskeletal tension (F_{actin}) are applied to integrin–ECM complexes presumably via talin. V_H increases integrin–ECM complexes and recruitment of talin and vinculin to FAs, thereby enhancing adhesive forces (F_{FA}) without influencing cytoskeletal tension. Full-length vinculin significantly enhances adhesive forces (F_{FA+CSK}) via (*i*) increasing integrin–FN complexes and talin and vinculin recruitment to FAs via V_H, and (*ii*) mechanical coupling these adhesive plaque complexes to the actin CSK. Mechanical coupling to CSK also enhances CSK tension. (*B*) Model for force-stabilized vinculin conformation. The vinculin molecule is maintained in its autoinhibited conformation via high-affinity head–tail interactions. Vinculin is activated into its open, active conformation by binding talin and actin. Force applied across the vinculin molecule stabilizes the open conformation of the molecule.

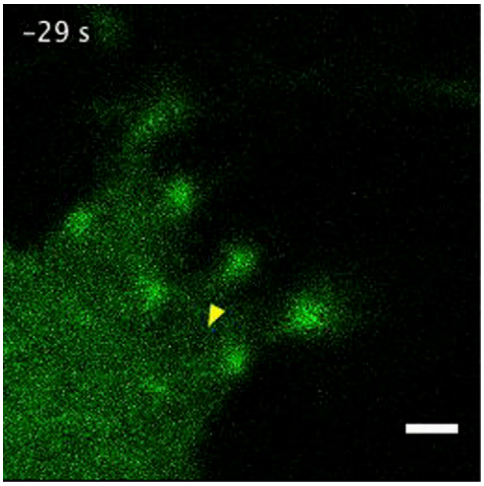

Movie S1. FRAP for WT vinculin at FAs under low applied force (FRAP-WT-3nN.avi). Movie shows fluorescence imaging of eGFP-WT expressing cells cultured on mPADs. A yellow arrow in the initial frame indicates magnitude and direction of force applied at FA (2.8 nN). A yellow circle indicates photobleached area.

Movie S1

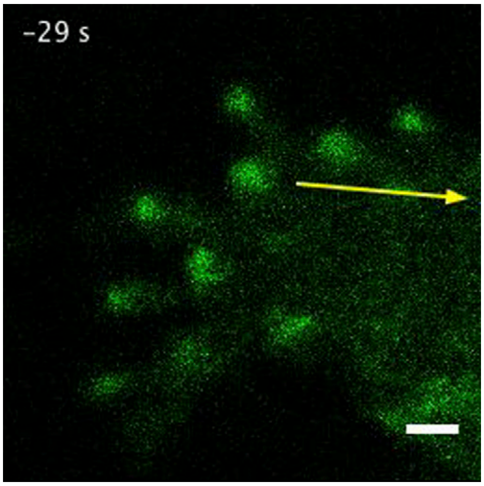

Movie S2. FRAP for WT vinculin at FAs under high applied force (FRAP-WT-29nN.avi). Movie shows fluorescence imaging of eGFP-WT expressing cells cultured on mPADs. A yellow arrow in the initial frame indicates magnitude and direction of force applied at FA (29 nN). A yellow circle indicates photobleached area.

Movie S2

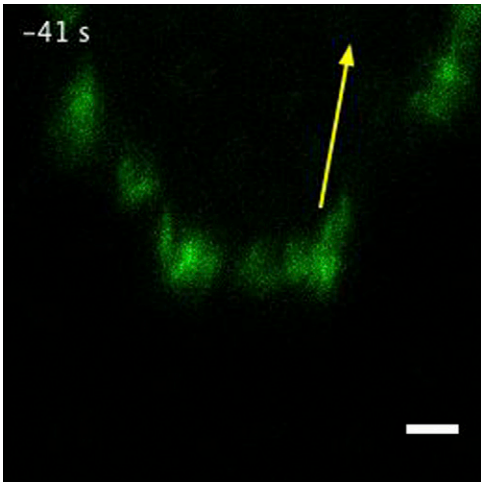

Movie S3. FRAP for T12 vinculin at FAs under high applied force (FRAP-T12-28nN.avi). Movie shows fluorescence imaging of eGFP-T12 expressing cells cultured on mPADs. A yellow arrow in the initial frame indicates magnitude and direction of force applied at FA (28.5 nN). A yellow circle indicates photobleached area.

Movie S3

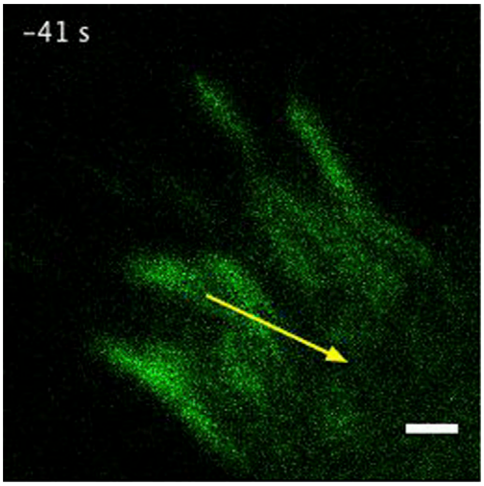

Movie S4. FRAP for V_H vinculin at FAs under high applied force (FRAP-VH-27nN.avi). Movie shows fluorescence imaging of eGFP-V_H expressing cells cultured on mPADs. A yellow arrow in the initial frame indicates magnitude and direction of force applied at FA (26.8 nN). A yellow circle indicates photobleached area.

Movie S4